

Single-exposure Fourier-transform ghost imaging based on spatial correlationZhijie Tan ¹, Hong Yu,^{1,2,*} Ruiguo Zhu ¹, Ronghua Lu,¹ Shensheng Han,^{1,2} Chaofan Xue,³ Shumin Yang,³ and Yanqing Wu³¹*Key Laboratory of Quantum Optics, Shanghai Institute of Optics and Fine Mechanics, Chinese Academy of Sciences, Shanghai 201800, China*²*Hangzhou Institute for Advanced Study, University of Chinese Academy of Sciences, Hangzhou 310024, China*³*Shanghai Synchrotron Radiation Facility, Shanghai Advanced Research Institute, Chinese Academy of Sciences, Shanghai 201204, China*

(Received 30 June 2022; accepted 1 November 2022; published 28 November 2022)

Ultrafast x-ray diffraction imaging provides an opportunity to realize x-ray nanoimaging of biomolecules before radiation damage, while the image resolution is still restricted by the photon flux. Fourier-transform ghost imaging based on the temporal intensity correlation can achieve diffraction-limited imaging. However, a large number of temporal samplings are inevitable, which makes it almost impossible to be implemented in the ultrafast x-ray imaging. Here, we propose an x-ray single-exposure Fourier-transform ghost imaging (SFGI) approach. The Fourier information of an unknown sample can be obtained by measuring the spatial intensity correlation between two speckle fields, and the sample needs to be exposed only once. In our demonstration experiment of SFGI, the Fourier-transform diffraction pattern of a two-dimensional sample is achieved, and its face-centered-cubic feature in the spatial domain is retrieved successfully. The simulation results of the DNA origami and rice dwarf virus indicate that a spatial resolution of 10 nm may be reached, and x-ray ghost imaging with 0.1 photon/pixel speckle detection can be expected. Our research paves the way for the future application of ultrafast x-ray ghost imaging.

DOI: [10.1103/PhysRevA.106.053521](https://doi.org/10.1103/PhysRevA.106.053521)**I. INTRODUCTION**

X-ray imaging is a powerful tool in materials science, biomedical research, and many other fields [1,2]. With the development of x-ray sources, such as x-ray free-electron lasers (XFEL) [3,4] and high-harmonic x-ray sources [5], it offers an opportunity for the ultrafast exploration of material nanostructures and biological macromolecules. X-ray coherent diffraction imaging (CDI) [6–8], a lensless imaging method, is famous for obtaining high-resolution images of noncrystalline samples with coherent light, which makes it especially suitable for XFEL applications. Recently, a single-particle imaging [9] method based on CDI has been proposed and the image of a virus sample has been achieved with XFEL [10]. However, as a diffraction imaging method exploiting the first-order coherence of optical fields, CDI requires a detector with very high dynamic range, and the x-ray photons are not fully utilized in the imaging process [11]. In the meantime, imaging technology based on the high-order coherence of optical fields, known as ghost imaging (GI) [12–14], has prospered in the past decades [15–17], and it has been rapidly applied in remote sensing, super-resolution imaging, single-pixel cameras, etc. [18–21]. Ghost imaging is a kind of indirect imaging technology which can extract the information of unknown samples by measuring the high-order correlation between the intensity fluctuations of optical fields.

This phenomenon was first observed in the quantum field [12,13]. Soon after, it was demonstrated with classical light sources [14,22], which makes GI more accessible. Nowadays, GI techniques have been extended to the x-ray regime [23–28], which shows the feasibility of imaging beyond the intrinsic diffraction limit [29,30] or under ultralow illumination [26,31].

X-ray ghost imaging can be realized in both real space [24–26] and reciprocal space [23,29]. In real-space x-ray GI, the image resolution is restricted by the optical components [32], and a large number of temporal measurements are required. Ghost imaging in reciprocal space, namely, Fourier-transform ghost imaging (FGI), was proposed in 2004 [33] and experimentally demonstrated using synchrotron x rays in 2016 [23]. In x-ray FGI, the same Fourier diffraction pattern as that in x-ray CDI can be achieved in a lensless way, reducing the requirements of spatial coherence and providing the possibility of nonlocal modulation, which provides the potential of high-resolution biomedical microscopy and material structure analysis. However, it suffers from massive temporal measurements as well. Even though various methods based on compressed sensing have been proposed to improve the sampling efficiency [34–36], thousands of temporal measurements are still needed to obtain a high-quality image. This brings a big challenge to x-ray applications, especially in the XFEL experiments, because nanoparticles are inevitably destroyed after single-shot exposure due to the high energy of XFEL pulses [37].

*yuhong@siom.ac.cn

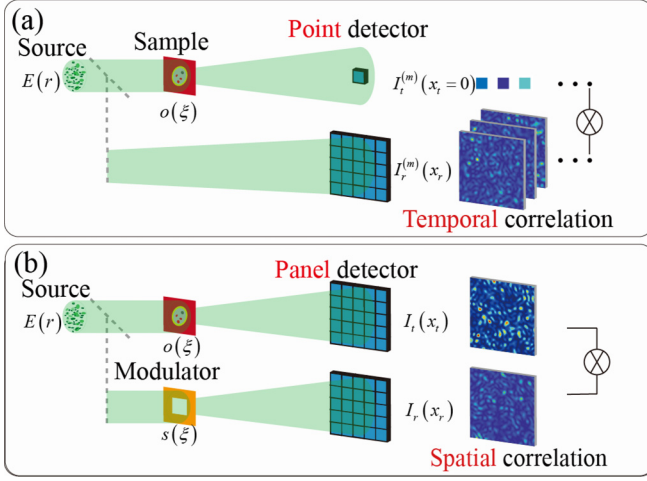


FIG. 1. Illustration of (a) x-ray Fourier-transform ghost imaging based on temporal correlation and (b) x-ray single-exposure Fourier-transform ghost imaging based on spatial correlation.

In this paper, we propose x-ray single-exposure Fourier-transform ghost imaging (SFGI): a lensless Fourier-transform imaging method based on the high-order spatial correlation of optical fields. By exploiting this spatial correlation characteristic, SFGI can greatly reduce the requirement for temporal samplings. Different from most x-ray ghost imaging techniques, the sample needs to be exposed only once during the SFGI imaging process, which makes it possible to be used in XFEL experiments. Relevant theoretical derivation and experimental results are presented. And the potential application of x-ray SFGI is discussed through exploratory simulation of the DNA origami and rice dwarf virus (RDV) imaging. We anticipate that this approach can pave the way for the realization of ultrafast high-resolution x-ray ghost imaging.

II. THEORY

The principle of basic x-ray FGI is shown in Fig. 1(a). A thermal or pseudothermal x-ray beam, the distribution of which satisfies the complex Gaussian distribution, is virtually divided into two beams by shifting the sample into and out of the optical path [23]. When the sample is inserted into the optical path, the x-ray intensity at a certain point on the detector plane is recorded as $I_t^{(m)}(x_t = 0)$. When the sample is moved out of the optical path, the x-ray speckle distribution on the detector plane is recorded as $I_r^{(m)}(x_r)$. The distance from the source to the sample is d_1 , and the distance from the sample to the detector is d_2 . After many measurements, the Fourier-transform diffraction pattern of the sample can be obtained by calculating the second-order correlation between

the temporal intensity fluctuations of the two beams, which can be expressed as [23,33]

$$\Delta G^{(2)}(x_r, x_t = 0) = \langle I_r(x_r)I_t(x_t = 0) \rangle - \langle I_r(x_r) \rangle \langle I_t(x_t = 0) \rangle \\ \propto \left| \int d\xi o(\xi) \exp\left(-j2\pi \frac{x_t - x_r}{\lambda d_2} \xi\right) \right|^2, \quad (1)$$

where $o(\xi)$ is the transmittance of the sample, λ is the x-ray wavelength, and the operation $\langle \cdot \rangle$ denotes the ensemble average, which is a temporal average over multiple intensity measurements.

Now we present our x-ray single-exposure Fourier-transform ghost imaging scheme. As illustrated in Fig. 1(b), a panel detector is adopted instead of a point detector to acquire the intensity distribution downstream of the sample, and a modulator is inserted into the optical path when the sample is moved out. In the imaging process, the sample is illuminated only once, and the Fourier information of the sample is extracted by calculating the spatial correlation between the two speckle distributions $I_t(x_t)$ and $I_r(x_r)$. This spatial correlation calculation is a spatial average over the intensity of pixel pairs between the two area detectors.

If we suppose the optical field on the source plane is represented by $E(r)$, the intensity distributions of the two beams on the detector plane can be written as

$$I_k(x_k) = \int dr_1 dr_2 E(r_1) E^*(r_2) h_k(r_1, x_k) h_k^*(r_2, x_k), \quad k = r, t, \quad (2)$$

where $h_t(r, x_t)$ and $h_r(r, x_r)$ are the impulse response functions of the two beams, and r and x_k are the coordinates of the source and detector planes, respectively. Under the paraxial approximation, we have

$$h_t(r, x_t) \propto \int d\xi \exp\left\{-\frac{j\pi}{\lambda d_1} (r - \xi)^2\right\} o(\xi) \\ \times \exp\left\{-\frac{j\pi}{\lambda d_2} (\xi - x_t)^2\right\}, \quad (3)$$

$$h_r(r, x_r) \propto \int d\xi \exp\left\{-\frac{j\pi}{\lambda d_1} (r - \xi)^2\right\} s(\xi) \\ \times \exp\left\{-\frac{j\pi}{\lambda d_2} (\xi - x_r)^2\right\}. \quad (4)$$

Here $s(\xi)$ is the transmittance of the modulator. Note that the modulator is inserted into the beam at the same position of the sample, so we can use the same variable ξ to denote the coordinates of the sample and modulator planes.

Then, we can calculate the second-order spatial intensity correlation between the two speckle fields, which is

$$G_{\text{Spatial}}^{(2)}(\Delta x = x_t - x_r) = \int I_t(x_r + \Delta x) I_r(x_r) dx_r \propto \int dr_1 dr_2 dr_3 dr_4 d\xi_1 d\xi_2 d\xi_3 d\xi_4 dx_r E(r_1) E^*(r_2) E(r_3) E^*(r_4) \\ \times \exp\left\{-\frac{j\pi}{\lambda d_1} \left[r_1^2 + \xi_1^2 - 2\xi_1 \left(r_1 + \frac{d_1}{d_2} x_r\right)\right]\right\} o(\xi_1) \exp\left\{\frac{j\pi}{\lambda d_1} \left[r_2^2 + \xi_2^2 - 2\xi_2 \left(r_2 + \frac{d_1}{d_2} x_r\right)\right]\right\} o^*(\xi_2) \\ \times \exp\left\{-\frac{j\pi}{\lambda d_1} \left[r_3^2 + \xi_3^2 - 2\xi_3 \left(r_3 + \frac{d_1}{d_2} x_r\right)\right]\right\} s(\xi_3) \exp\left\{-\frac{j\pi}{\lambda d_2} \xi_3^2\right\}$$

$$\begin{aligned}
& \times \exp \left\{ \frac{j\pi}{\lambda d_1} \left[r_4^2 + \xi_4^2 - 2\xi_4 \left(r_4 + \frac{d_1}{d_2} x_r \right) \right] \right\} s^*(\xi_4) \exp \left\{ \frac{j\pi}{\lambda d_2} \xi_4^2 \right\} \\
& \times \exp \left\{ -\frac{j\pi}{\lambda d_2} (\xi_1^2 - 2\xi_1 \Delta x) \right\} \exp \left\{ \frac{j\pi}{\lambda d_2} (\xi_2^2 - 2\xi_2 \Delta x) \right\}.
\end{aligned} \quad (5)$$

Define $R = r + (d_1/d_2)x_r$, $x = (d_1/d_2)x_r$, and let $A(r) = E(r) \times \exp\{-j\pi r^2/(\lambda d_1)\}$. In many cases, the field fluctuations of the source can be described by a complex circular Gaussian ergodic random process with zero mean [38]. The integral on variable x can be regarded as a spatial averaging process, and then we have

$$\begin{aligned}
& \int dx A(R_1 - x) A^*(R_2 - x) A(R_3 - x) A^*(R_4 - x) \\
& = G_S^{(1)}(R_1, R_2) G_S^{(1)}(R_3, R_4) + G_S^{(1)}(R_1, R_3) G_S^{(1)}(R_2, R_4),
\end{aligned} \quad (6)$$

where $G_S^{(1)}$ denotes the first-order spatial intensity correlation function. If we suppose the source is large enough and the feature size of the fluctuations is small enough, $G_S^{(1)}$ can be treated as a Delta function.

Substituting Eq. (6) into Eq. (5), after some calculations, we obtain the following expression:

$$\begin{aligned}
& \Delta G_{\text{Spatial}}^{(2)}(\Delta x = x_r - x_r) \\
& = \int I_r(x_r) I_t(x_r + \Delta x) dx_r - \int dx_r I_r(x_r) \int dx_t I_t(x_t) \\
& \propto \left| \int d\xi o(\xi) s^*(\xi) \exp\left(-j2\pi \frac{x_r - x_r}{\lambda d_2} \xi\right) \right|^2.
\end{aligned} \quad (7)$$

Therefore, by means of the second-order spatial correlation calculation, the Fourier information of the sample modulated by the modulator can be achieved. It should be mentioned that when the feature size of the fluctuation is not small enough, the image quality will deteriorate.

Simply using an aperture no smaller than the sample as the modulator, the correlation result will be the Fourier-transform diffraction pattern of the sample. Moreover, we know from the above that the sample can be nonlocally modulated by the modulator. This implies that the sample and the modulator can be exposed separately. This feature is the same as the nonlocally coded FGI based on temporal correlation, which provides the possibility of achieving better image quality [39,40].

In addition, the Fourier-transform pattern of the squared modulus of the sample's transmittance can be obtained through the spatial autocorrelation calculation. This means that only one exposure is needed to obtain the sample's amplitude and phase information separately, which can also be exploited to improve the image quality [23,41].

III. EXPERIMENTS

The experiment was carried out on the 08U1B beamline at the Shanghai Synchrotron Radiation Facility [42]. The

fundamental photon energy of the beamline ranged from 85 to 150 eV, and the whole system operated in vacuum.

Figure 2 shows the schematic layout of our experiment. A 4.2-m-long APPLE-II type elliptically polarized undulator with 100-mm periods produced extreme ultraviolet or soft-x-ray photons. A four-blade aperture (Slit1) with the size of 1100 μm was placed in the optical path to define the acceptance angle of the beam. Two cylindrical mirrors (CM1 and CM2) were employed to focus the beam horizontally and vertically, and suppress the high-order harmonics [43]. The second four-blade aperture (Slit2) positioned at the focus of the cylindrical mirrors was used to balance the spatial coherence and brightness of the beam. In the experiment, the size of Slit2 was set to 33 μm , and the total flux was 2.6×10^{14} photons/s. The distance from Slit2 to the diffuser was 9 m, and the theoretical coherence width of the light on the diffuser plane was 3.65 mm at 92.5 eV. As shown in the subgraph of Fig. 2, the diffuser adopted in the experiment was a gold film with randomly distributed holes. The diameter of the holes was 200 nm, which is significantly larger than the wavelength, and the area duty ratio of the holes was about 18%. Using the diffuser, a controllable speckle field with random intensity fluctuation was generated. The sample and modulator were mounted on an electric translation stage, which can move them into and out of the optical path remotely. At the end of the beam, the x-ray intensity distribution was recorded by an Andor CCD camera with a pixel size of 13 μm . We first investigated the characteristics of the speckle field. A $50 \times 50 \mu\text{m}^2$ square aperture was inserted into the optical path as a working modulator. The distance from the diffuser to the aperture was $d_1 = 4$ cm, and the distance from the aperture

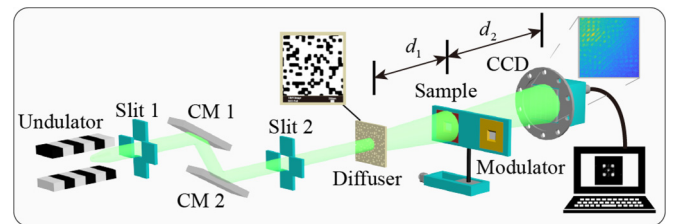


FIG. 2. Schematic layout of the single-exposure Fourier-transform ghost imaging experiment. The beam emitted from the undulator propagates from left to right. Slit1 and Slit2 are two four-blade apertures. CM1 and CM2 are two cylindrical mirrors. The diffuser is a gold film with randomly distributed holes. The subgraph shows the scanning electron microscope image of the diffuser. An electric translation stage moves the sample and modulator into and out of the beam remotely. A CCD camera is placed at the end of the beam to record speckle fields. By calculating the spatial correlation between speckle fields, the Fourier-transform diffraction pattern of the sample can be obtained, and then the real-space image of the sample is retrieved.

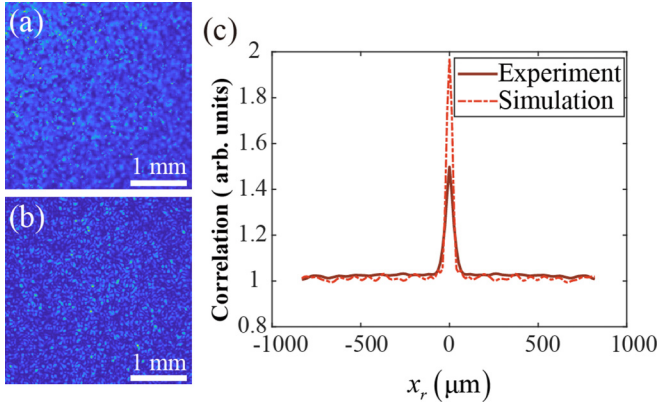


FIG. 3. Investigation on the characteristics of the speckle field with a $50 \times 50 \mu\text{m}^2$ square aperture in the optical path. (a) Intensity distribution obtained by experiment. (b) Intensity distribution obtained by simulation. (c) Autocorrelation results calculated from the speckle patterns in (a) and (b). 256×256 pixels were used in each calculation

to the CCD was $d_2 = 16$ cm. Figure 3 displays the results. Figure 3(a) is the intensity distribution obtained in the experiment. We did some regular filtering to reduce the noise in the raw image. Median filtering was used to reduce salt and pepper noise, and morphological filtering was adopted to reduce uneven background noise. Figure 3(b) gives the corresponding simulation result for comparison. It can be observed that the statistical characteristics of the experimental speckle is similar to the simulation result. The average speckle size in Fig. 3(a) is very close to that in Fig. 3(b). For quantitative evaluation, the autocorrelation functions of the speckle fields were calculated. According to the convolution theorem [44], the spatial correlation operation was performed in the Fourier domain for simplicity. We used 256×256 pixels in the speckle image in each calculation. The results are shown in Fig. 3(c). The two curves in Fig. 3(c) have similar correlation peaks, and the full width at half maximum (FWHM) of the two curves are almost the same. The measured FWHM is 4 pixels ($4 \times 13 \mu\text{m} = 52 \mu\text{m}$), and the difference from the theoretical value is less than 1 pixel.

After the speckle field investigation, we inserted a sample into the beam. The sample was a gold film with 35 slits on a Si_3N_4 substrate. The slits were separated by $d_{\text{slit}} = 1.4 \mu\text{m}$ and the width of each slit was $0.5 \mu\text{m}$. The total width of the 35 slits was $49.5 \mu\text{m}$, which was equivalent to the size of the aperture modulator. Figure 4 gives the imaging results of this slits sample. Figure 4(a) is the intensity distribution obtained with the sample in the optical path. The spatial correlation between the sample beam and the modulator beam was calculated following Eq. (7). The solid line in Fig. 4(b) shows the cross-section curve of the spatial correlation result. The Fourier-transform diffraction peaks of the sample are very clear. The peak spacing is $4.5 \mu\text{m}^{-1}$, which is consistent with the theoretical value of the peak spacing $2\pi/d_{\text{slit}} = 4.49 \mu\text{m}^{-1}$. Thus, the sample's Fourier-transform diffraction pattern can be achieved by spatial correlation calculation with the sample exposed only once in the imaging process.

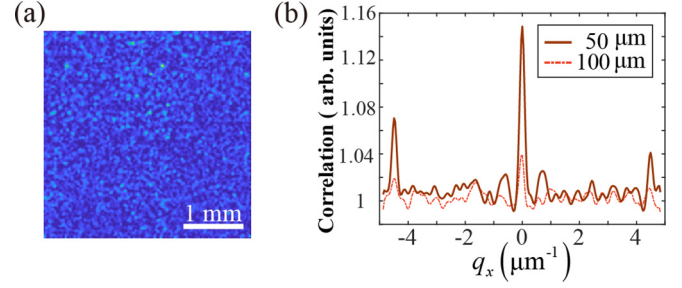


FIG. 4. Experimental results of a slits sample. (a) Intensity distribution obtained with the slits sample inserted into the beam. (b) Cross-section curves of the spatial correlation results. The solid and dashed lines correspond to the correlation results of the 50- and 100- μm aperture modulators, respectively.

It can be seen from Eq. (7) that using a modulator smaller than the sample size may lose information of the sample. Theoretically, when the spatial sampling is sufficient, increasing the modulator size has no influence on the imaging results. However, due to the restriction of the detector size or photon flux, the spatial sampling is usually limited in practical applications. When the spatial sampling is insufficient, the pattern quality will decline. In order to verify this effect, we inserted a 100- μm aperture modulator into the beam, and calculated the spatial correlation between the sample beam and the modulator beam again. The result is shown by the dashed line in Fig. 4(b). In this case, the diffraction peaks of the sample are almost submerged in the background noise. This is because the larger the modulator size, the smaller the speckle size will be. The size of the speckle produced by the 100- μm aperture is smaller than that produced by the 50- μm aperture. Thus, to obtain the same pattern quality, the number of the spatial samplings for the 100- μm aperture modulator should be increased several times accordingly. In the experiment, the spatial sampling of 256×256 pixels remained, so the correlation results deteriorated. Therefore, to achieve better results in practice, the size of the modulator should approach the size of the sample. This prevents the loss of sample information and avoids extra sampling requirements. Finally, a two-dimensional (2D) sample was inserted into the beam to further test our method. The sample consisted of five circular holes, which mimics the face of a typical face-centered-cubic structure. The diameter of the four surrounding holes was $2.6 \mu\text{m}$, and the diameter of the central hole was $1.4 \mu\text{m}$. The distance from the central hole to the center of the surrounding hole was $4 \mu\text{m}$. The sample was fabricated on a Si_3N_4 substrate, and the total size of the sample was about $10 \mu\text{m}$. Figure 5(a) displays the scanning electron microscope image of the sample. Figure 5(b) is the intensity distribution obtained in the experiment. The exposure time was 700 s. As mentioned above, the Fourier-transform diffraction pattern of the sample can be obtained by calculating the second-order spatial correlation function. The correlation result is shown in Fig. 5(c). Figure 5(d) is the real-space image of the sample retrieved from the diffraction pattern in Fig. 5(c). The features of the image are obviously in agreement with the sample. Here, the phase recovery process consists of two steps. First, the relaxed averaged alternating reflections algorithm [45] was

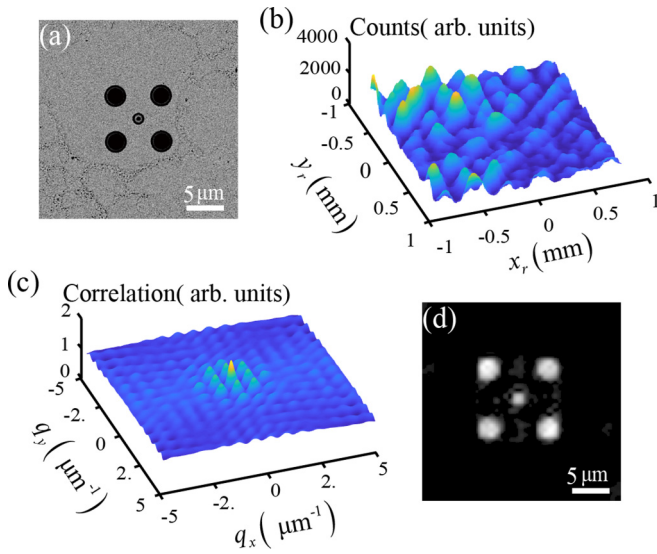


FIG. 5. Experimental results of a two-dimensional sample. (a) Scanning electron microscope image of the sample. (b) Intensity distribution obtained with the sample positioned in the beam. (c) Fourier-transform diffraction pattern of the sample obtained by spatial correlation calculation. (d) Real-space image of the sample retrieved from the diffraction pattern in (c).

adopted, and the relaxation parameter was set to 0.8. We calculated 100 runs, and each run started with a random initial guess. The iteration number for each run was 200. After all the 100 runs, we chose the image with the least error as the template. Secondly, we implemented the difference map (DM) algorithm [46] with the obtained template. The relaxation parameter and the iteration number used in the DM algorithm were 0.8 and 200, respectively.

There are some points we should mention. In order to avoid the influence of the high-order harmonics in the beam, the sample was moved slightly away from the optical axis. This is not required in the SFGI experiment with monochromatic light. In our experiment, a diffuser was used to generate the x-ray spatial intensity fluctuation, but sometimes it may be unnecessary. To demonstrate our method, we use a simple square aperture as the modulator. In practice, the modulator can be specifically designed to obtain coded diffraction patterns, and better image quality can be expected, especially for complex samples. Considering the fabrication difficulty, a binary mask may be a feasible choice. Theoretically, three different binary masks are sufficient to obtain precise phase retrieval results [39,40].

IV. SIMULATIONS

To explore the potential of biological application in the future, we conducted some proof-of-concept numerical simulations. The DNA origami icosahedra and rice dwarf virus were used as samples in our simulation.

Figure 6 presents the simulation results of the DNA origami icosahedra. Figure 6(a) shows the three-dimensional nanoscale geometry of the DNA origami scaffold. It was generated by the online open-source DAEDALUS software developed by the Laboratory of Computational Biology and

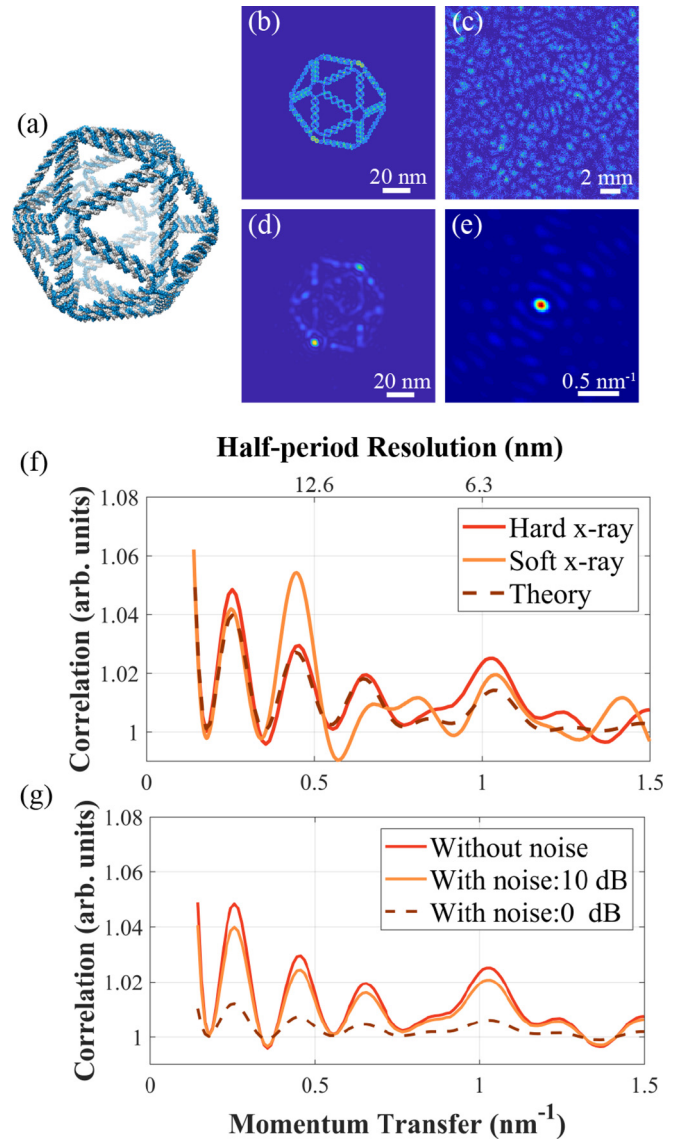


FIG. 6. Simulation results of DNA origami icosahedra. (a) Three-dimensional nanoscale geometry of the DNA origami scaffold. The length of each edge is 52 base pairs (≈ 17 nm). (b) Two-dimensional projection of the DNA origami in a specific orientation. The scale bar is 20 nm. (c) Speckle distribution on the detector plane. The average photon number for each pixel is one photon. The scale bar is 2 mm. (e) Diffraction pattern obtained by spatial correlation calculation. The scale bar is 0.5 nm^{-1} . (d) Retrieved image. The scale bar is 20 nm. (f) Radial profile of the diffraction pattern compared with the theoretical value. (g) Noise influence on the radial profile of the diffraction pattern.

Biophysics at MIT [47]. An icosahedral structure with 52 base pairs on each edge was synthesized, and the length of each edge was approximately 17 nm. The atom types and positions were used to calculate the complex refractive index, and then the transmittance of the DNA origami can be obtained [48,49].

In our simulation, an x-ray field with random phase distribution was generated as a start. The energy of x-ray photons is 8 keV (0.15 nm). Then the sample was simulated and illuminated by the x-ray field. After exposure, the photon (intensity) distribution on the detecting plane was

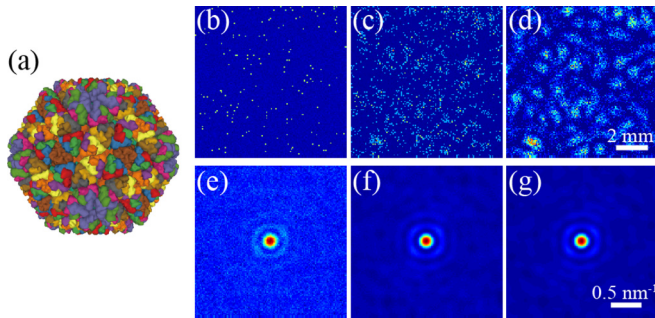


FIG. 7. Simulation results of RDV. (a) Atomic structure of RDV. (b, c, d) Speckle patterns of 0.01, 0.1, and 1 photon/pixel, respectively. (e, f, g) Spatial correlation results corresponding to the speckle patterns in (b), (c), and (d).

calculated according to the scattering propagation formula [50]. The distance from the sample to the detector was 66.7 cm. The pixel size of the detector used in the simulation was $75\ \mu\text{m}$, which is the same as that used in the single-particle imaging experiment at the Linac Coherent Light Source [51]. The analog-to-digital units count per photon was 130, which means a photon can be detected with a count of 130. To make the simulation results reflect the experimental data, random noise with Gaussian distribution was added to the simulation data. The noise was estimated on the basis of the pixel rms of the detector and set to 2.6 digital units according to practical devices [52]. Using the obtained photon distribution on the detector, the diffraction pattern of the sample was obtained through the second-order spatial correlation calculation. Finally, the sample structure in real space was retrieved by the phase retrieval algorithm described in the experimental section.

Figure 6(b) shows the 2D projection of the DNA origami in a specific orientation. Figure 6(c) is a cropped image of the simulated speckle distribution recorded by the detector, and the size of the image is 128×128 pixels. The average photon number for each pixel is 1 photon. The diffraction pattern obtained by spatial autocorrelation calculation is shown in Fig. 6(e). We used 4096×4096 pixels in the calculation. Figure 6(d) is the result recovered from Fig. 6(e). It is quite similar to the original image of the 2D projection in Fig. 6(b). For better evaluation, the radial profile of the diffraction pattern is given in Fig. 6(f) as a function of momentum transfer. With the increase of momentum transfer, the simulation curve deviates from the theoretical value. A half-period resolution of about 10 nm may be achieved with the development of the diffuser fabrication technology. Simulation with soft x rays (1 keV) was also performed. The distance from the sample to the detector was 40 cm, and the result is shown in Fig. 6(f). It can be found that the spatial resolution will reduce to about 20 nm. Figure 6(g) shows the influence of noise. The result is acceptable while the single-to-noise ratio is 10 dB. As the noise increases, the contrast of the diffraction pattern will decrease and the image quality will deteriorate.

Figure 7 presents the simulation results of RDV. Figure 7(a) is the atomic structure of the RDV sample, which can

be read from the protein data bank (PDB ID:1UF2) [53,54]. We performed simulations to investigate the influence of the intensity of the detected speckles. The simulation process of RDV is the same as that of the DNA origami. The speckle patterns of different photon numbers obtained on the detector plane are shown in Figs. 7(b)–7(d). The photon numbers are 0.01, 0.1, and 1 photon/pixel, respectively. Figures 7(e)–7(f) are the corresponding spatial correlation results obtained from the speckle patterns in Figs. 7(b)–7(d). The results are displayed on a logarithmic scale. The structural similarity (SSIM) index [55] between Figs. 7(f) and 7(g) is 0.99, which means the results of 0.1 and 1 photon/pixel are almost the same. However, the SSIM between Figs. 7(e) and 7(g) is only 0.32. This implies that when the intensity of the detected speckle is 0.01 photon/pixel, the quality of the diffraction pattern decreases dramatically, and it will be difficult to retrieve the sample structure in the spatial domain.

V. CONCLUSION

In summary, we have proposed an x-ray single-exposure Fourier-transform ghost imaging approach, which overcomes the obstacle of a large amount of temporal samplings in most x-ray ghost imaging, and shows the feasibility of using the advanced x-ray sources to realize ultrafast x-ray ghost imaging. It is proved theoretically that the Fourier information of an unknown sample can be obtained by measuring the spatial intensity correlation between two speckle fields, and the sample needs to be exposed only once in x-ray SFGI. We demonstrate the SFGI method with synchrotron radiation. In the experiment, the Fourier-transform diffraction pattern of a two-dimensional sample with face-centered-cubic feature was achieved, and the spatial distribution of the sample was successfully retrieved. Relevant simulation results of the DNA origami and rice dwarf virus are provided to show the potential of SFGI in high-resolution x-ray microscopy of biological samples. According to the simulation, a spatial resolution of 10 nm may be reached, and x-ray ghost imaging with 0.1 photon/pixel speckle detection can be expected.

SFGI is a lensless Fourier imaging method, and its theoretical resolution is only limited by the wavelength. To obtain better image resolution in practice, substantial spatial samplings are needed, which may result in an increased demand for the illumination flux. Incorporating compressive sensing or deep learning technology to extract the sample information more effectively will be helpful. It is worth mentioning that SFGI offers a more flexible scheme to improve image quality. Since the sample can be nonlocally encoded by the modulator, the image quality can be enhanced [39]. This feature is significant to the x-ray imaging of biological samples.

ACKNOWLEDGMENTS

This work was supported by National Natural Science Foundation of China (Grants No. 11627811 and No. 11775286) and National Key Research and Development Program of China (Grants No. 2017YFB0503303 and No. 2017YFB0503300). The authors thank the staff of the BL08U beamline at Shanghai Synchrotron Radiation Facility.

APPENDIX A: THEORETICAL DERIVATION

Here we provide a detailed derivation from Eq. (5) to Eq. (7). We first simplify the formula (5) as follows:

$$\begin{aligned}
G_{\text{Spatial}}^{(2)}(\Delta x = x_t - x_r) &\propto \int dr_1 dr_2 dr_3 dr_4 d\xi_1 d\xi_2 d\xi_3 d\xi_4 dx_r \\
&\times E(r_1) \exp\left\{-\frac{j\pi}{\lambda d_1}\left[r_1^2 + \xi_1^2 - 2\xi_1\left(r_1 + \frac{d_1}{d_2}x_r\right)\right]\right\} o(\xi_1) \exp\left\{-\frac{j\pi}{\lambda d_2}(\xi_1^2 - 2\xi_1 \Delta x)\right\} \\
&\times E^*(r_2) \exp\left\{\frac{j\pi}{\lambda d_1}\left[r_2^2 + \xi_2^2 - 2\xi_2\left(r_2 + \frac{d_1}{d_2}x_r\right)\right]\right\} o^*(\xi_2) \exp\left\{\frac{j\pi}{\lambda d_2}(\xi_2^2 - 2\xi_2 \Delta x)\right\} \\
&\times E(r_3) \exp\left\{-\frac{j\pi}{\lambda d_1}\left[r_3^2 + \xi_3^2 - 2\xi_3\left(r_3 + \frac{d_1}{d_2}x_r\right)\right]\right\} s(\xi_3) \exp\left\{-\frac{j\pi}{\lambda d_2}\xi_3^2\right\} \\
&\times E^*(r_4) \exp\left\{\frac{j\pi}{\lambda d_1}\left[r_4^2 + \xi_4^2 - 2\xi_4\left(r_4 + \frac{d_1}{d_2}x_r\right)\right]\right\} s^*(\xi_4) \exp\left\{\frac{j\pi}{\lambda d_2}\xi_4^2\right\}. \tag{A1}
\end{aligned}$$

Define $R = r + (d_1/d_2)x_r$, $x = (d_1/d_2)x_r$, and let $A(r) = E(r) \times \exp\{-j\pi r^2/(\lambda d_1)\}$. The value of the Jacobian determinant is a constant d_1/d_2 . So we have the following expression:

$$\begin{aligned}
G_{\text{Spatial}}^{(2)}(\Delta x = x_t - x_r) &\propto \int dR_1 dR_2 dR_3 dR_4 d\xi_1 d\xi_2 d\xi_3 d\xi_4 dx \\
&\times A(R_1 - x) \exp\left\{-\frac{j\pi}{\lambda d_1}(\xi_1^2 - 2\xi_1 R_1)\right\} o(\xi_1) \exp\left\{-\frac{j\pi}{\lambda d_2}(\xi_1^2 - 2\xi_1 \Delta x)\right\} \\
&\times A^*(R_2 - x) \exp\left\{\frac{j\pi}{\lambda d_1}(\xi_2^2 - 2\xi_2 R_2)\right\} o^*(\xi_2) \exp\left\{\frac{j\pi}{\lambda d_2}(\xi_2^2 - 2\xi_2 \Delta x)\right\} \\
&\times A(R_3 - x) \exp\left\{-\frac{j\pi}{\lambda d_1}(\xi_3^2 - 2\xi_3 R_3)\right\} s(\xi_3) \exp\left\{-\frac{j\pi}{\lambda d_2}\xi_3^2\right\} \\
&\times A^*(R_4 - x) \exp\left\{\frac{j\pi}{\lambda d_1}(\xi_4^2 - 2\xi_4 R_4)\right\} s^*(\xi_4) \exp\left\{\frac{j\pi}{\lambda d_2}\xi_4^2\right\}. \tag{A2}
\end{aligned}$$

Substituting Eq. (6) into Eq. (A2), we obtain

$$\begin{aligned}
G_{\text{Spatial}}^{(2)}(\Delta x = x_t - x_r) &\propto \int dR_1 dR_3 d\xi_1 d\xi_2 d\xi_3 d\xi_4 \exp\left\{-\frac{j\pi}{\lambda d_1}(\xi_1^2 - \xi_2^2 + \xi_3^2 - \xi_4^2)\right\} \\
&\times \exp\left\{-\frac{j\pi}{\lambda d_1}2R_1(\xi_2 - \xi_1)\right\} \exp\left\{-\frac{j\pi}{\lambda d_1}2R_3(\xi_4 - \xi_3)\right\} \\
&\times o(\xi_1)s^*(\xi_4) \exp\left\{-\frac{j\pi}{\lambda d_2}(\xi_1^2 - \xi_4^2 - 2\xi_1 \Delta x)\right\} \times o^*(\xi_2)s(\xi_3) \exp\left\{\frac{j\pi}{\lambda d_2}(\xi_2^2 - \xi_3^2 - 2\xi_2 \Delta x)\right\} \\
&+ \int dR_1 dR_3 d\xi_1 d\xi_2 d\xi_3 d\xi_4 \exp\left\{-\frac{j\pi}{\lambda d_1}(\xi_1^2 - \xi_2^2 + \xi_3^2 - \xi_4^2)\right\} \\
&\times \exp\left\{-\frac{j\pi}{\lambda d_1}2R_1(\xi_4 - \xi_1)\right\} \exp\left\{-\frac{j\pi}{\lambda d_1}2R_3(\xi_2 - \xi_3)\right\} \\
&\times o(\xi_1)s^*(\xi_4) \exp\left\{-\frac{j\pi}{\lambda d_2}(\xi_1^2 - \xi_4^2 - 2\xi_1 \Delta x)\right\} \times o^*(\xi_2)s(\xi_3) \exp\left\{\frac{j\pi}{\lambda d_2}(\xi_2^2 - \xi_3^2 - 2\xi_2 \Delta x)\right\} \\
&= \int d\xi |o(\xi)|^2 \int d\xi |s(\xi)|^2 + \left| \int d\xi o(\xi)s^*(\xi) \exp\left(-j2\pi \frac{x_t - x_r}{\lambda d_2} \xi\right) \right|^2. \tag{A3}
\end{aligned}$$

The first term is a constant background, which is proportional to $\int dx_r I_r(x_r) \int dx_t I_t(x_t)$. The second term contains the Fourier information of the sample modulated by the modulator. From above, Eq. (7) can be achieved.

APPENDIX B: DIFFUSER AND SAMPLE FABRICATION

The patterns of the diffuser and the sample were generated through electron-beam lithography. The fabrication process started with a Si_3N_4 membrane, the thickness of the membrane was 100 nm, and the size was $1 \times 1 \text{ mm}^2$. Then the resist layer was spin coated on it from a resist solution (6% of 350-k PMMA in ethyl-lactate) at 3000 rpm for 60 s followed by a soft bake at 180°C for 5 min. The pattern exposure was carried out on a 100-keV electron-beam writer (JEOL 6300FS) at 500-pA beam current. The development was performed by immersing the exposed chip in a mixture of isopropanol and water (7:3 by volume) for 3 min followed by rinsing in deionized water for 30 s and drying in a N_2 gas jet. The Au metal was filled into the PMMA mold by electroplating. Finally, the PMMA was stripped in solvents after plating.

The thickness of the diffuser was 67 nm and the thickness of the sample was 300 nm. In fabrication, this thickness difference was achieved by controlling the electroplating time.

APPENDIX C: SAMPLE SIMULATION

The atom types and positions of the sample used in the simulation were obtained from the public atom data. The

scattering length density D_{SL} can be calculated via

$$D_{\text{SL}} = \frac{\rho N_a \sum_{i=1}^N b_i}{\sum_{i=1}^N M_i}, \quad (\text{C1})$$

where N_a is the Avogadro number, M_i is the atomic molar mass for each element, and ρ is the density of the sample. The scattering length b_i indicates the scattering ability of the i th atom. The relationship between scattering length density and refractive index $n = 1 - \delta + i\beta$ can be described as follows:

$$\delta = \frac{\lambda^2}{2\pi} \text{Re}D_{\text{SL}}, \quad (\text{C2a})$$

$$\beta = \frac{\lambda^2}{2\pi} \text{Im}D_{\text{SL}}. \quad (\text{C2b})$$

Thus, we can achieve the complex refractive index of the sample from the atom data.

In our simulation, the sample was divided into $128 \times 128 \times 128$ volumes, and we obtained the three-dimensional complex refractive index of the sample according to the above description. Then the sample was projected into two-dimensional space, and the two-dimensional complex amplitude distribution of the sample was calculated and used in the simulation.

-
- [1] A. Sakdinawat and D. Attwood, Nanoscale x-ray imaging, *Nat. Photonics* **4**, 840 (2010).
- [2] H. N. Chapman and K. A. Nugent, Coherent lensless x-ray imaging, *Nat. Photonics* **4**, 833 (2010).
- [3] C. Pellegrini, A. Marinelli, and S. Reiche, The physics of x-ray free-electron lasers, *Rev. Mod. Phys.* **88**, 015006 (2016).
- [4] H. M. Quiney and K. A. Nugent, Biomolecular imaging and electronic damage using x-ray free-electron lasers, *Nat. Phys.* **7**, 142 (2011).
- [5] Y. Pertot, C. Schmidt, M. Matthews, A. Chauvet, M. Huppert, V. Svoboda, A. von Conta, A. Tehlar, D. Baykusheva, J.-P. Wolf *et al.*, Time-resolved x-ray absorption spectroscopy with a water window high-harmonic source, *Science* **355**, 264 (2017).
- [6] J. Miao, T. Ishikawa, I. K. Robinson, and M. M. Murnane, Beyond crystallography: Diffractive imaging using coherent x-ray light sources, *Science* **348**, 530 (2015).
- [7] D. Sayre, H. Chapman, and J. Miao, On the extendibility of x-ray crystallography to noncrystals, *Acta Crystallogr. Sect. A* **54**, 232 (1998).
- [8] J. Miao, P. Charalambous, J. Kirz, and D. Sayre, Extending the methodology of x-ray crystallography to allow imaging of micrometre-sized non-crystalline specimens, *Nature (London)* **400**, 342 (1999).
- [9] A. Aquila, A. Barty, C. Bostedt, S. Boutet, G. Carini, D. DePonte, P. Dreier, S. Doniach, K. Downing, T. Earnest *et al.*, The linac coherent light source single particle imaging road map, *Struct. Dyn.* **2**, 041701 (2015).
- [10] R. P. Kurta, J. J. Donatelli, C. H. Yoon, P. Berntsen, J. Bielecki, B. J. Daurer, H. DeMirici, P. Fromme, M. F. Hantke, F. R. N. C. Maia, A. Munke, C. Nettelblad, K. Pande, H. K. N. Reddy, J. A. Sellberg, R. G. Sierra, M. Svenda, G. van der Schot, I. A. Vartanyants, G. J. Williams, Correlations in Scattered X-Ray Laser Pulses Reveal Nanoscale Structural Features of Viruses, *Phys. Rev. Lett.* **119**, 158102 (2017).
- [11] S. Teichmann, B. Chen, R. A. Dilanian, P. Hannaford, and L. Van Dao, Experimental aspects of multiharmonic-order coherent diffractive imaging, *J. Appl. Phys.* **108**, 023106 (2010).
- [12] T. B. Pittman, Y. H. Shih, D. V. Strekalov, and A. V. Sergienko, Optical imaging by means of two-photon quantum entanglement, *Phys. Rev. A* **52**, R3429 (1995).
- [13] D. V. Strekalov, A. V. Sergienko, D. N. Klyshko, and Y. H. Shih, Observation of Two-Photon “Ghost” Interference and Diffraction, *Phys. Rev. Lett.* **74**, 3600 (1995).
- [14] A. Valencia, G. Scarcelli, M. D’Angelo, and Y. Shih, Two-Photon Imaging with Thermal Light, *Phys. Rev. Lett.* **94**, 063601 (2005).
- [15] J. H. Shapiro and R. W. Boyd, The physics of ghost imaging, *Quant. Info. Proc.* **11**, 949 (2012).
- [16] P.-A. Moreau, E. Toninelli, T. Gregory, and M. J. Padgett, Ghost imaging using optical correlations, *Laser Photonics Rev.* **12**, 1700143 (2018).
- [17] T. J. Lane and D. Ratner, What are the advantages of ghost imaging? multiplexing for x-ray and electron imaging, *Opt. Express* **28**, 5898 (2020).
- [18] W. Gong, C. Zhao, H. Yu, M. Chen, W. Xu, and S. Han, Three-dimensional ghost imaging lidar via sparsity constraint, *Sci. Rep.* **6**, 1 (2016).
- [19] S. Gazit, A. Szameit, Y. C. Eldar, and M. Segev, Super-resolution and reconstruction of sparse sub-wavelength images, *Opt. Express* **17**, 23920 (2009).
- [20] M. F. Duarte, M. A. Davenport, D. Takhar, J. N. Laska, T. Sun, K. F. Kelly, and R. G. Baraniuk, Single-pixel imaging

- via compressive sampling, *IEEE Signal Process. Mag.* **25**, 83 (2008).
- [21] P. Ryczkowski, M. Barbier, A. T. Friberg, J. M. Dudley, and G. Genty, Ghost imaging in the time domain, *Nat. Photonics* **10**, 167 (2016).
- [22] A. Gatti, E. Brambilla, M. Bache, and L. A. Lugiato, Ghost Imaging with Thermal Light: Comparing Entanglement and Classical Correlation, *Phys. Rev. Lett.* **93**, 093602 (2004).
- [23] H. Yu, R. Lu, S. Han, H. Xie, G. Du, T. Xiao, and D. Zhu, Fourier-Transform Ghost Imaging with Hard X Rays, *Phys. Rev. Lett.* **117**, 113901 (2016).
- [24] D. Pelliccia, A. Rack, M. Scheel, V. Cantelli, and D. M. Paganin, Experimental X-Ray Ghost Imaging, *Phys. Rev. Lett.* **117**, 113902 (2016).
- [25] A. Schori and S. Shwartz, X-ray ghost imaging with a laboratory source, *Opt. Express* **25**, 14822 (2017).
- [26] A.-X. Zhang, Y.-H. He, L.-A. Wu, L.-M. Chen, and B.-B. Wang, Tabletop x-ray ghost imaging with ultra-low radiation, *Optica* **5**, 374 (2018).
- [27] A. M. Kingston, D. Pelliccia, A. Rack, M. P. Olbinado, Y. Cheng, G. R. Myers, and D. M. Paganin, Ghost tomography, *Optica* **5**, 1516 (2018).
- [28] Y. Y. Kim, L. Gelisio, G. Mercurio, S. Dziarzhytski, M. Beye, L. Bocklage, A. Classen, C. David, O. Y. Gorobtsov, R. Khubbutdinov *et al.*, Ghost imaging at an XUV free-electron laser, *Phys. Rev. A* **101**, 013820 (2020).
- [29] R. Schneider, T. Mehringer, G. Mercurio, L. Wenthous, A. Classen, G. Brenner, O. Gorobtsov, A. Benz, D. Bhatti, L. Bocklage *et al.*, Quantum imaging with incoherently scattered light from a free-electron laser, *Nat. Phys.* **14**, 126 (2018).
- [30] J.-E. Oh, Y.-W. Cho, G. Scarcelli, and Y.-H. Kim, Sub-Rayleigh imaging via speckle illumination, *Opt. Lett.* **38**, 682 (2013).
- [31] W.-K. Yu, X.-F. Liu, X.-R. Yao, C. Wang, G.-J. Zhai, and Q. Zhao, Single-photon compressive imaging with some performance benefits over raster scanning, *Phys. Lett. A* **378**, 3406 (2014).
- [32] T. A. Smith, Y. Shih, Z. Wang, X. Li, B. Adams, M. Demarteau, R. Wagner, J. Xie, L. Xia, R.-Y. Zhu *et al.*, From optical to x-ray ghost imaging, *Nucl. Instrum. Methods Phys. Res., Sect. A* **935**, 173 (2019).
- [33] J. Cheng and S. Han, Incoherent Coincidence Imaging and Its Applicability in X-ray Diffraction, *Phys. Rev. Lett.* **92**, 093903 (2004).
- [34] O. Katz, Y. Bromberg, and Y. Silberberg, Compressive ghost imaging, *Appl. Phys. Lett.* **95**, 131110 (2009).
- [35] W.-K. Yu, M.-F. Li, X.-R. Yao, X.-F. Liu, L.-A. Wu, and G.-J. Zhai, Adaptive compressive ghost imaging based on wavelet trees and sparse representation, *Opt. Express* **22**, 7133 (2014).
- [36] V. Katkovnik and J. Astola, Compressive sensing computational ghost imaging, *J. Opt. Soc. Am. A* **29**, 1556 (2012).
- [37] H. N. Chapman, C. Caleman, and N. Timneanu, Diffraction before destruction, *Phil. Trans. R. Soc. B* **369**, 20130313 (2014).
- [38] J. W. Goodman, *Statistical Optics* (Wiley, New York, 2015).
- [39] Z. Tan, H. Yu, R. Lu, R. Zhu, S. Yang, and S. Han, Non-locally coded Fourier-transform ghost imaging, *Opt. Express* **27**, 2937 (2019).
- [40] E. J. Candes, X. Li, and M. Soltanolkotabi, Phase retrieval from coded diffraction patterns, *Appl. Comput. Harmonic Anal.* **39**, 277 (2015).
- [41] G. Ying, Q. Wei, X. Shen, and S. Han, A two-step phase-retrieval method in Fourier-transform ghost imaging, *Opt. Commun.* **281**, 5130 (2008).
- [42] C. Xue, X. Meng, Y. Wu, Y. Wang, L. Wang, S. Yang, J. Zhao, and R. Tai, The wave optical whole process design of the soft x-ray interference lithography beamline at SSRF, *J. Synchrotron Radiat.* **25**, 1869 (2018).
- [43] C. Xue, Y. Wu, F. Zhu, S. Yang, H. Liu, J. Zhao, L. Wang, and R. Tai, Development of broadband x-ray interference lithography large area exposure system, *Rev. Sci. Instrum.* **87**, 043303 (2016).
- [44] J. W. Goodman, *Introduction to Fourier Optics* (Roberts & Co., Englewood, Colorado, 2005).
- [45] D. R. Luke, Relaxed averaged alternating reflections for diffraction imaging, *Inverse Probl.* **21**, 37 (2005).
- [46] V. Elser, Phase retrieval by iterated projections, *J. Opt. Soc. Am. A* **20**, 40 (2003).
- [47] R. Veneziano, S. Ratanalert, K. Zhang, F. Zhang, H. Yan, W. Chiu, and M. Bathe, Designer nanoscale dna assemblies programmed from the top down, *Science* **352**, 1534 (2016).
- [48] Z. Sun, J. Fan, H. Li, H. Liu, D. Nam, C. Kim, Y. Kim, Y. Han, J. Zhang, S. Yao *et al.*, Necessary experimental conditions for single-shot diffraction imaging of dna-based structures with x-ray free-electron lasers, *ACS Nano* **12**, 7509 (2018).
- [49] M. Bergh, G. Huldt, N. Timneanu, F. R. Maia, and J. Hajdu, Feasibility of imaging living cells at subnanometer resolutions by ultrafast x-ray diffraction, *Q. Rev. Biophys.* **41**, 181 (2008).
- [50] D. Rupp, L. Flückiger, M. Adolph, A. Colombo, T. Gorkhover, M. Harmand, M. Krikunova, J. P. Müller, T. Oelze, Y. Ovcharenko *et al.*, Imaging plasma formation in isolated nanoparticles with ultrafast resonant scattering, *Struct. Dyn.* **7**, 034303 (2020).
- [51] H. K. Reddy, C. H. Yoon, A. Aquila, S. Awel, K. Ayyer, A. Barty, P. Berntsen, J. Bielecki, S. Bobkov, M. Bucher *et al.*, Coherent soft x-ray diffraction imaging of coliphage PR772 at the linac coherent light source, *Sci. Data* **4**, 170079 (2017).
- [52] A. Munke, J. Andreasson, A. Aquila, S. Awel, K. Ayyer, A. Barty, R. J. Bean, P. Berntsen, J. Bielecki, S. Boutet *et al.*, Coherent diffraction of single rice dwarf virus particles using hard x-rays at the linac coherent light source, *Sci. Data* **3**, 160064 (2016).
- [53] D. Sehnal, A. Rose, J. Koca, S. Burley, and S. Velankar, Mol*: Towards a common library and tools for web molecular graphics, in *Proceedings of the Workshop on Molecular Graphics and Visual Analysis of Molecular Data, Brno, Czech Republic* (2018), pp. 29–33.
- [54] A. Nakagawa, N. Miyazaki, J. Taka, H. Naitow, A. Ogawa, Z. Fujimoto, H. Mizuno, T. Higashi, Y. Watanabe, T. Omura *et al.*, The atomic structure of rice dwarf virus reveals the self-assembly mechanism of component proteins, *Structure* **11**, 1227 (2003).
- [55] Z. Wang, A. C. Bovik, H. R. Sheikh, and E. P. Simoncelli, Image quality assessment: From error visibility to structural similarity, *IEEE Trans. Image Process.* **13**, 600 (2004).